

Different shapes of spin textures as a journey through the Brillouin zone

Carlos Mera Acosta^{1,2},[✉] Linding Yuan,¹ Gustavo M. Dalpian,² and Alex Zunger^{1,*}

¹*Renewable and Sustainable Energy Institute, University of Colorado, Boulder, Colorado 80309, USA*

²*Center for Natural and Human Sciences, Federal University of ABC, Santo Andre, São Paulo, Brazil*



(Received 1 July 2021; accepted 2 July 2021; published 7 September 2021)

Crystallographic point group symmetry (CPGS) such as polar and nonpolar crystal classes have long been known to classify compounds that have spin-orbit-induced spin splitting. While taking a journey through the Brillouin zone (BZ) from one k -point to another for a fixed CPGS, it is expected that the wave vector point group symmetry (WPGS) can change, and consequently, a qualitative change in the texture of the spin polarization can occur [the expectation value of spin operator \vec{S}_{nk_0} in Bloch state $u(n, k)$ and the wave vector k_0]. However, the nature of the spin texture (ST) change is generally unsuspected. In this paper, we determine a full classification of the linear-in- k ST patterns based on the polarity and chirality reflected in the WPGS at k_0 . The spin-polarization vector \vec{S}_{nk_0} controlling the ST is bound to be parallel to the rotation axis and perpendicular to the mirror planes, and hence, symmetry operation types in WPGSs impose symmetry restriction to the ST. For instance, the ST is always parallel to the wave vector k in nonpolar chiral WPGSs since they contain only rotational symmetries. Some consequences of the ST classification based on the symmetry operations in the WPGS include the observation of ST patterns that are unexpected according to the symmetry of the crystal. For example, it is usually established that spin-momentum locking effect (spin vector always perpendicular to the wave vector) requires the crystal inversion symmetry breaking by an asymmetric electric potential. However, we find that polar WPGS can have this effect even in compounds without electric dipoles or external electric fields. We use the determined relation between WPGS and ST as a design principle to select compounds with multiple STs near band edges at different k valleys. Based on high-throughput calculations for 1481 compounds, we find 37 previously fabricated materials with different STs near band edges. The ST classification as well as the predicted compounds with multiple STs can be a platform for potential application for spin-valleytronics and the control of the ST by accessing different valleys.

DOI: [10.1103/PhysRevB.104.104408](https://doi.org/10.1103/PhysRevB.104.104408)

I. INTRODUCTION

Whereas symmetry generally allows or forbids numerous effects in solid state and molecular science, a recurring question is: What aspect of group symmetries is responsible for given types of phenomena? For example, symmetries contained in the crystallographic point group symmetry (CPGS) establish the enabling conditions for macroscopic properties, such as electric polarization [1], magnetization [2], circular dichroism [3], and pyroelectricity [4]. The CPGS is, however, insufficient to universally describe all material properties in crystals. In fact, wave-vector-dependent effects are enabled by other elements of symmetry such as the wave vector point group symmetry (WPGS)—the little point group (PG) of specific wave vectors k_0 in the Brillouin zone (BZ). For instance, symmetry protection of exotic fermions [5,6] and energy band anticrossing [7] depends on the WPGS. The Zeeman-type spin splitting (SS) [8,9] is an example of enabling physical mechanisms that seem to contradict the macroscopic crystal symmetry. Specifically, in contrast to the Zeeman effect in magnetic compounds, the Zeeman-type effect is observed in nonmagnetic compounds [i.e., CPGS preserving the time-reversal (TR) symmetry] but at k -points with WPGS breaking

the TR symmetry. Naturally, effects enabled by the CPGS are only allowed at those special wave vectors at which the two symmetries coincide (WPGS = CPGS). However, it is expected that other wave vectors lead to very different effects.

Overlooking the distinction between different physics enabled by WPGS vs that enabled by the CPGS has often created an incompleteness of the symmetry classification of spin-related phenomena and their wave vector dependence. A curious historical development in this regard has been the association of the CPGS with the texture of the spin-polarization \vec{S}_{nk_0} —the expectation values of spin operators \hat{S}_i in a given Bloch wave function $u(n, k)$ that is centered at a specific k_0 with n referring to a Bloch band. Specifically, Fig. 1 illustrates different shapes of spin textures (STs) that have been observed, including radial ST ($\vec{S}_{nk} \parallel \vec{k}$) [10–12], tangential ST ($\vec{S}_{nk_0} \perp \vec{k}$) [13–15], or the tangential-radial ST [16,17]. These observations were generally established for highly specific wave vectors k_0 that satisfy WPGS = CPGS, e.g., the Γ point in GaAs ($F\bar{4}3m$) [16] and the Z point in GeTe ($R\bar{3}m$) [13,14]. For this reason, ST shapes were often associated with the presence or absence of crystallographic inversion symmetry in the CPGS, rather than with the WPGS of the specific wave vector k_0 . Furthermore, when different ST shapes were noted in different functional materials, it was tempting to associate the specific ST with the underlying functionality. For instance, the observation of tangential ST in some

*acosta@if.usp.br

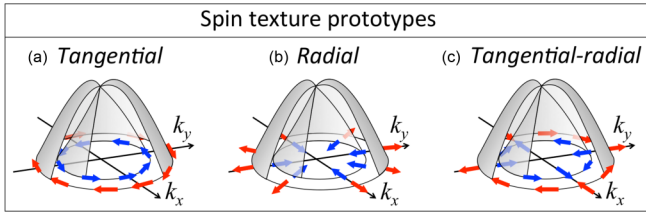


FIG. 1. Schematic representation of the (a) tangential texture $\vec{S}_{nk} \perp \vec{k}$, (b) radial texture $\vec{S}_{nk} \parallel \vec{k}$, and (c) tangential-radial texture at a two-dimensional plane k_{xy} normal to a rotation axis R_i .

ferroelectrics has been associated with the physics of electric polarization [14,18,19]. However, not all ferroelectrics have such a ST type [20]. Similarly, the observation of tangential ST in some topological insulators has been associated with their topological character; however, normal insulators can also have this very same ST [21].

In $\mathbf{k} \cdot \mathbf{p}$ effective Hamiltonians $\mathcal{H}(k \rightarrow k_0)$, for wave vectors k around the origin k_0 of the expansion, the ST is properly determined by the little PG of wave vector k_0 [22,23]. However, despite extensive applications of the $\mathbf{k} \cdot \mathbf{p}$ effective Hamiltonians to study STs for wave vectors k_0 , associations of the resulting ST behavior with the CPGS rather than the WPGS abound. For example, the tangential ST [Fig. 1(b)] seen in bulk compounds is often associated with the Rashba physics of breaking the crystallographic inversion symmetry via asymmetric electric potentials (i.e., electric field or bulk electric polarization) [24], rather than with the WPGS of the wave vector studied. Although it is properly expected that, while taking a journey through the BZ from one point k_0 to another, the k vector symmetry and the thus the ST might qualitatively change, the nature of the change is generally unsuspected. This position was clearly expressed in a recent paper studying the radial ST of Weyl fermions in chiral tellurium [11], concluding that “A full classification of the spin vector field geometry is beyond the scope of this study, and it will be the subject of a future investigation.”

This paper discusses a direct resolution of the classification problem of STs. We show that the enabling symmetries underlying the ST types are not a reflection of material functionalities, nor are they caused by the presence or absence of polar fields in the CPGS [24]. Instead, ST shapes are caused by a symmetry principle cutting across different material functionalities: the existence of specific proper (rotations) and improper symmetries (reflections and inversion) in the WPGS (a subgroup of the CPGS). Specifically, we show that the spin-polarization vector \vec{S}_{nk_0} controlling the ST is bound to be parallel to the rotation axis and perpendicular to the mirror planes. This imposes a prediction on the ensuing ST patterns according to the polarity and chirality of the k_0 WPGS. For example, for k_0 with nonpolar chiral WPGS having more than one rotation symmetry and no mirror symmetry, we expect \vec{S}_{nk_0} to be parallel to the rotation axis, i.e., that $\vec{S}_{nk_0}(k) \parallel \vec{k}$. Here, chiral (nonchiral) PGs have only proper (both proper and improper) symmetries, while polar (nonpolar) PGs have one (more than one) rotation axis. Thus, a journey throughout the BZ of a fixed compound reveals ST types corresponding to different rotation and reflection symmetries of the little group of k . For instance, we expect (and confirm) that compounds

with nonpolar crystallographic symmetry (i.e., without electric dipoles or electric fields) can show the tangential ST (i.e., Rashba-like ST) at the wave vector k_0 whose WPGS is polar. This illustrates that the breaking of the inversion symmetry mediated by an electric dipole or external electric field being a defining feature of Rashba effect is not a necessary condition for the Rashba ST (Fig. 1), contrary to what is generally assumed by the macroscopic CPGS and used to investigate the formation of spin spirals [24–27] for different classes of materials.

Understanding the association of ST with the WPGS (rather than with the wave-vector-independent CPGS) could be a productive basis for design of compounds with target ST and its control by accessing different valleys in the BZ. Thus, we explore the potential application to spin-valleytronics of the proposed journey throughout the BZ to access multiple ST types in the same compound. The application of our study is based on the inverse design approach [28] for the selection of compounds with single and cofunctionalities [7,20]. Contrary to the direct approach based on the calculation for all possible material candidates, the inverse design aims first to establish the physical mechanisms [or design principles (DPs)] behind the target property, i.e., compounds with multiple ST shapes in the BZ. In the second step of this approach, the DPs are used as filters for the screening of compounds from known material databases, e.g., the AFLOW-Inorganic Crystal Structure Database (ICSD) [29]. In the first step, for BZs of three-dimensional (3D) noncentrosymmetric (NCS) Bravais lattices, we apply the relations between the ST shapes and the WPGS polarity and chirality, determining all possible symmetrically allowed WPGSs in all 21 NCS CPGSs (i.e., 139 crystallographic space groups). Only polar nonchiral, nonpolar chiral, and nonpolar nonchiral CPGSs can have CPGS allowing high-symmetry k -points with different STs. Based on the CPGS and WPGS, we select 1481 fabricated compounds and perform high-throughput density functional theory (DFT) band structure calculations for them. Focusing on band structures in which the relative energy at different valleys is <100 meV and SS >1 meV, we identify 37 compounds with multiple ST shapes. Examples include nonpolar chiral SiO_2 ($P6_322$), CPGS = D_6 , that have radial ST at the high-symmetry point A (WPGS = CPGS) and tangential-radial ST at the high-symmetry point H (WPGS = D_3). The SSs at these k -points are 26 and 6 meV, respectively. The proposed classification of the ST based on the WPGS and the selected compounds in the inverse design process is a potential platform for spin-valleytronics applications.

II. CLASSIC $\mathbf{k} \cdot \mathbf{p}$ HAMILTONIANS USED TO PROVIDE THE ST TYPE FOR THE SPECIAL CASE OF WPGS = CPGS

We next illustrate three linear-in- k relativistic Hamiltonians (Rashba, Weyl, and Dresselhaus) set to a specific wave vector k_0 with WPGS = CPGS, which is not representative of other parts of the BZ, as summarized in Table I. Figure 2 shows the DFT-calculated STs at different wave vectors k_0 with both WPGS = CPGS and WPGS \neq CPGS for the representative compounds described in Table I.

Rashba and collaborators established that “if a crystal has a single high-symmetry axis (at least threefold),” [30–32], i.e.,

TABLE I. When the WPGS of k_0 equals the global CPGS, i.e., k_0 with WPGS = CPGS (shown here for GaAs, GeTe, and Te), then ST type has the highest symmetry, but a journey through the BZ shows the more typical cases where k_0 has WPGS \neq CPGS, leading to many different types of STs.

Compounds	CPGS	k_0 with WPGS = CPGS	ST for k_0 with WPGS = CPGS	k_0 with WPGS \neq CPGS	ST for k_0 with WPGS \neq CPGS
GeTe ($R3m$)	C_{3v}	$\Gamma (C_{3v}), Z(C_{3v})$	Rashba	$L(C_s)$	Dresselhaus-Rashba
Te ($P3_121$)	D_3	$\Gamma (T), A(T_d)$	Weyl	$M(C_2)$	Undefined
GaAs ($F\bar{4}3m$)	T_d	$\Gamma (T_d)$	Dresselhaus	$L(C_{3v})$	Rashba

crystals with polar CPGS, spin bands are described by the linear-in- k spin-orbit coupling (SOC) Hamiltonian:

$$\mathcal{H}_R(k \rightarrow k_0) = \lambda_R(k_x \sigma_y - k_y \sigma_x),$$

where the z component of the momentum \vec{k} is set along the high-symmetry axis, and σ_i are the Pauli matrixes. The

Hamiltonian \mathcal{H}_R was historically used to study both two-dimensional (2D) compounds with perpendicular electric fields and heterojunctions with interfacial electric dipoles. In these systems, only wave vectors k_0 with WPGS = CPGS (e.g., $k_0 = \Gamma$) satisfy the Hamiltonian \mathcal{H}_R . The diagonal-

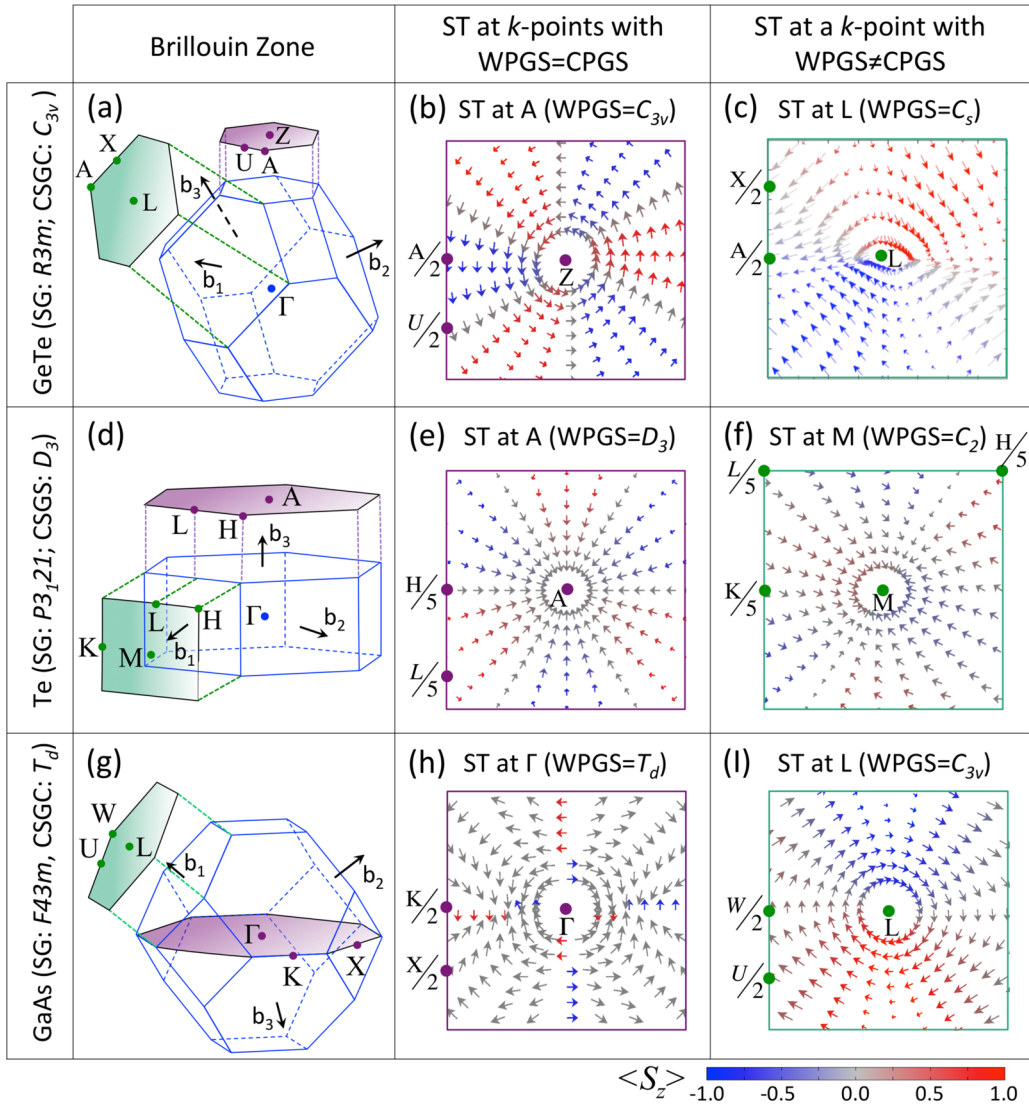


FIG. 2. Variations of density functional theory (DFT)-calculated spin texture (ST) prototypes at different wave vector point group symmetries (WPGSs) viewed as a journey through the Brillouin zone (BZ) of fixed given compounds. We show the BZ for (a) GeTe, (d) tellurium, and (g) GaAs, which are, respectively, nonpolar, polar, and chiral compounds according to their crystallographic point group symmetry (CPGS). The journey departure points for (b) GeTe, (e) Te, and (h) GaAs are wave vectors k_0 that have a point group symmetry equal to the macroscopic CPGS, so the STs are the ones expected from the CPGS, i.e., tangential ST for GeTe, radial ST for Te, and tangential-radial ST for GaAs. However, shifting to k -points of lower wave vector symmetries [(c), (f), and (i), respectively] shows greatly altered ST shapes for the same compounds.

ization of \mathcal{H}_R leads to the tangential ST (i.e., \vec{S}_{nk} always perpendicular to the momentum ($\vec{S}_{nk_0}(k) \perp \vec{k}$) or equivalently $\vec{S}_{nk_0}(k) = (-k_y, k_x, 0)/|\vec{k}|$), which is usually referred to as Rashba ST or spin-momentum locking effect. In the 3D analog, i.e., the bulk Rashba effect, compounds with polar CPGS [e.g., BiTeI ($R3m$) and GeTe ($R3m$)] [13,15,33], have an intrinsic nonzero electric dipole that effectively plays the role of the interfacial dipole in heterojunctions. As shown in the first line of Table I, in GeTe ($R3m$), the BZ wave vector $k_0 = Z$ has the Rashba-like ST, as illustrated via relativistic DFT calculations in Fig. 2(b). This spin-momentum locking effect is also observed in the surface states near the Γ point of the BZ of 3D topological insulators [34].

In crystals with chiral CPGS, at wave vectors k_0 with WPGS = CPGS, spin bands are described by the effective Hamiltonian:

$$\mathcal{H}_w(k \rightarrow k_0) = \lambda_w(k_x\sigma_x + k_y\sigma_y),$$

which was proposed by Weyl [35]. The diagonalization of \mathcal{H}_w results in the radial ST (i.e., the spin always parallel to the wave vector $\vec{S}_{nk_0}(k) \parallel \vec{k}$, or equivalently $\vec{S}_{nk_0}(k) = (k_x, k_y, 0)/|\vec{k}|$), which is historically known as Weyl ST. As shown in the second line of Table I, in the two equivalently chiral enantiomers of bulk tellurium ($P3_121$ and $P3_221$) [10–12], at the high-symmetry k -points Γ and A (with WPGS = CPGS), the Weyl ST is observed [Fig. 2(e)]. The Hamiltonian \mathcal{H}_w also describes topological Weyl semimetals [36,37].

In compounds with nonpolar CPGS, Dresselhaus [38] determined that, for $k_0 = \Gamma$ (WPGS = CPGS), spin bands are described by the Hamiltonian

$$H_D = \lambda[(k_y^2 - k_z^2)k_xJ_x + (k_z^2 - k_x^2)k_yJ_y + (k_x^2 - k_y^2)k_zJ_z],$$

where J_i are the components of the total angular momentum operator, and k_z is fixed along a rotation axis R_i in the BZ. In the normal plane to R_i , the linear-in- k Hamiltonian is given by the Dresselhaus term:

$$\mathcal{H}_D(k \rightarrow k_0) = \lambda_D(k_x\sigma_x - k_y\sigma_y).$$

The diagonalization of \mathcal{H}_D leads to the tangential-radial ST [i.e., $\vec{S}(n, k_0) = (k_x, -k_y, 0)$], which is usually known as Dresselhaus ST. In the third line of Table I, we present GaAs ($F\bar{4}3m$) with nonpolar CPGS T_d , at $k_0 = \Gamma$ (WPGS = T_d) as a historical example of the Dresselhaus ST, as illustrated via quantitative relativistic DFT calculations in Fig. 2(h).

Hereafter, we will refer to \mathcal{H}_R , \mathcal{H}_w , and \mathcal{H}_D as linear-in- k SOC Rashba, Weyl, and Dresselhaus Hamiltonians, respectively. The STs resulting from these Hamiltonians are routinely observed in specific high-symmetry k -points with WPGS = CPGS of compounds with nonpolar CPGS (such as the Γ point in GaAs ($F\bar{4}3m$) [16] and IrBiSe ($P213$) [17]) and compounds with polar CPGS (such as the Z point in GeTe ($R3m$) [13,14] and BiTeI ($P3m1$) [15]).

III. k_0 DEPENDENT EFFECTS ARE REFLECTED IN THE WPGS, WHEREAS MACROSCOPIC SYMMETRY EFFECTS ARE REFLECTED IN THE CPGS

A journey through wave vectors in a BZ can visit symmetries different than the macroscopic CPGS. Specifically,

for each CPGS, there exists another layer of symmetries of wave vectors k_0 (shown in Table I) in the corresponding BZ [39–41]. This layer of symmetries consists of subgroups of the CPGS and enables specific momentum and band-dependent properties in the crystal such as band crossing, anticrossing [42], topological band inversion [43–45], and topological protection [46]. The inspection of STs at other k -points reveals patterns that are not predicted by the CPGS. For instance, for the traditional ferroelectric compound GeTe ($R3m$) with Rashba ST at $k_0 = Z$ (polar WPGS and CPGS) [47], Fig. 2(c) shows the ST obtained from the same relativistic calculation in Fig. 2(b), but this time at another wave vector $k_0 = L$ (first line in Table I). The ST reveals a pattern that is not a Rashba-like ST [Fig. 2(c)]. Likewise, in bulk Te, Fig. 2(e) presents the traditional Weyl ST at $k_0 = A$, which is deformed in another wave vector $k_0 = M$, showing an apparently undefined pattern [Fig. 2(f)]. We will discuss this undefined pattern in the next sections. Finally, for the nonpolar compound GaAs with Dresselhaus ST at $k_0 = \Gamma$ (WPGS = CPGS), Fig. 2(i) shows the typical Rashba-like ST obtained quantitatively from the same relativistic band structures used in Fig. 2(b), but this time at another wave vector $k_0 = L$. The latter example of GaAs illustrates a Rashba ST in a compound without electric dipoles (i.e., compound with nonpolar CPGS). Additionally, in contrast to the previous suggestion that Rashba ST is attributed to an intrinsic electric dipole and strong atomistic SOC [48], we see that, even with relatively weak atomic SOC in the GaAs, the spin can be perpendicular to the momentum k [Fig. 2(i)].

Interestingly, despite the potential applications in spintronics and valleytronics, the general description of how the little group of k vectors determines the spin-polarization pattern has remained unappreciated. Indeed, the full classification of the spin vector field geometry is an open problem [11]. The common characterization of ST patterns in terms of the CPGS (e.g., the existence or absence of electric polarization [49]) applies only for WPGS $\mathcal{G}(k)$ equal to the CPGS (e.g., the Γ point in all lattices, or the Z point in the BZ of GeTe), as shown in Table I. From the examples of ST prototypes in GeTe, Te, and GaAs (Table I and Fig. 2), we can directly anticipate some physical consequences: (i) The existence of different symmetries of wave vectors k_0 in the BZ leads to the possibility of having more than one spin-polarization prototype pattern in the same compound. This suggests that a ST assignment based only on the CPGS can lead to a misclassification of the ST shapes. (ii) Compounds without electric dipoles can have Rashba-like ST [Fig. 2(i)], meaning that contrary to what has been traditionally established, the asymmetry of the electric polarization is not a necessary condition for the Rashba ST.

IV. DERIVATION OF THE RELATION BETWEEN THE POINT GROUP OF THE k -POINT AND SPIN-POLARIZATION PATTERNS

Examples of the connection between the WPGS in the BZ and macroscopic properties include the notion of “elementary band representation” proposed by Zak [50–52], and its extension [43] including SOC that distinguishes compounds having symmetry-protected topological phases. Inspired by this idea, we investigate how specific symmetry operations in the WPGS $\mathcal{G}^*(k)$ imposes rules on the \vec{S}_{nk} . These symmetry

TABLE II. Character table of the double PG C_{3v} [53]. The headers are the symmetry operations contained in the PG C_{3v} , namely, the identity E , the threefold rotation symmetry R_3 , the diagonal mirror plane M_σ , and the TR symmetry τ . For each irreducible representation ($\gamma = A_1, A_2, E, E_{1/2}, {}^1E_{3/2}$, and ${}^2E_{3/2}$), the characters are shown.

C_{3v}	E	$2R_3$	$3M_\sigma$	τ
A_1	1	1	1	a
A_2	1	1	-1	a
E	2	-1	0	a
$E_{1/2}$	2	1	0	c
${}^1E_{3/2}$	1	-1	i	b
${}^2E_{3/2}$	1	-1	$-i$	b

operations contained in WPGS $\mathcal{G}^*(k)$ can be orientation-preserving symmetries termed first kind, such as rotations R_m of an angle $\theta = 2\pi/m$ (with m being an integer), or orientation-reversing symmetries (e.g., reflections M_i and roto-inversions) termed second kind [4]. We use two equivalent approaches to establish the relation between little PGs $\mathcal{G}^*(k)$ and ST shapes for a given wave vector k_0 , namely, A . We derive the linear-in- k SOC Hamiltonian $\mathcal{H}(k \rightarrow k_0)$ for all possible WPGS in the BZ of NCS compounds. After diagonalizing all Hamiltonian prototypes, the eigenvectors $\psi_n(k)$ are then used to calculate the expectation value $\langle S_{nk_0}(k) \rangle$ and B . based on the symmetry transformation properties of pseudovectors, we determine how the specific proper and improper symmetry operations determine the direction of the spin-polarization.

A. Linear-in- k SOC Hamiltonian for WPGS in the BZ of NCS compounds

The symmetry operations contained in a specific WPGS $\mathcal{G}^*(k)$ induce a set of irreducible representations $\gamma_m(d_m)$, which are described in the character table of the PG $\mathcal{G}^*(k)$ [53]. Here, d_m is the dimension of the representation γ_m , which in turn corresponds to the trace of identity symmetry operation E . In Table II, the character table of the PG C_{3v} is represented. Using the symmetry operators in a given basis (the matrix form of the symmetry operators), one can then evaluate under which irreducible representation of $\mathcal{G}^*(k)$ a specific object or property P is transformed. For instance, in Table III, the irreducible representations of functions $f_{\gamma_n}(k)$ and Pauli matrices σ_i are shown for irreducible representations $\gamma_{1,2} = A_{1,2}$ and $\gamma_3 = E$. In general, bands at the wave vector k_0 can also be characterized by the irreducible representations γ_m of the PG $\mathcal{G}^*(k_0)$. If a band n transforms under the irre-

ducible representation γ_m , the dimension d_m correspond to the degeneracy of the given band.

The Hamiltonian must be invariant, so it transforms under the identity irreducible representations γ_1 —the representation in which all characters are one (e.g., the representation A_1 for the PG C_{3v} in Table II). From the tables of the direct product of representations [53], we see that the tensor product $\gamma_m \otimes \gamma_m$ has usually at least one scalar that transforms according to identity irreducible representations γ_1 . The Hamiltonian can thus be constructed by considering the sum of products between a function $f_{\gamma_n}(k)$ and a basis matrix X_{γ_m} [e.g., Pauli matrices σ_i ($i = 0, 1, 2, 3$) are the basis for Hermitical matrices with $n = 2$] that transform under the same irreducible representation γ_m . For instance, for a two-band effective Hamiltonian, e.g., one orbital with spin \uparrow and \downarrow , we have

$$\mathcal{H}(k) = \sum_{m,i} c_m f_{\gamma_n}^i(k) \sigma_i^{\gamma_m} \delta_{nm},$$

where c_m are real coefficients. As an illustrative example of these products, we use the PG C_{3v} . For example, σ_z transforms under the irreducible representation $\gamma_2 = A_2$ (Table III), and there are no functions $f_{A_2}(k)$ that transform under the representation γ_2 , so there are no terms obtained from the product $\gamma_2 \otimes \gamma_2$ in the Hamiltonian. Considering all products containing Pauli matrices that are even under the TR symmetry, the resulting Hamiltonian for $\mathcal{G}^*(k_0) = C_{3v}$ is given by

$$\mathcal{H}(k \rightarrow k_0) = c_1 \mathbb{1}k^2 + c_3(k_x \sigma_y - k_y \sigma_x), \quad (1)$$

where $k^2 = k_x^2 + k_y^2 + k_z^2$. The physical interpretation of the Hamiltonian allows us to directly determine the coefficients c_m . The first term of the Hamiltonian is obtained from $\gamma_1 \otimes \gamma_1$ (with $\gamma_1 = A_1$) and gives the kinetic energy, meaning that $c_1 = -\hbar/2m^*$. Similarly, the second term in Eq. (1) (obtained from $\gamma_3 \otimes \gamma_3$ with $\gamma_3 = E$) corresponds to the linear-in- k Rashba SOC Hamiltonian \mathcal{H}_R with $c_3 = \lambda_R$. This simple analysis not only allows us to determine that the Rashba Hamiltonian \mathcal{H}_R is symmetrically allowed in the WPGS $\mathcal{G}^*(k_0) = C_{3v}$, but it also indicates that the Weyl and Dresselhaus Hamiltonians are symmetrically forbidden. A detailed description of this method can be found in Ref. [22]. This method of invariants has been used to study the linear-in- k Rashba SOC Hamiltonians allowed by the symmetry operations of polar PGs, as well as the high-order contributions to the Rashba-Bychkov effect [54,55]. Here, we extend this approach to determine the effective SOC Hamiltonian for all possible wave vector PGs $\mathcal{G}^*(k_0)$ that are NCS.

Figure 3 summarizes all SOC Hamiltonians that are symmetrically allowed by the specific WPGSs $\mathcal{G}^*(k_0)$, which

TABLE III. Cartesian tensors σ_i and s, p, d , and f functions ($l = 0, 1, 2$, and 3) [53].

C_{3v}	0	1	2	3
A_1	$\mathbb{1}_{2 \times 2}$	k_z	$k_x^2 + k_y^2, k_z^2$	$k_x(3k_x^2 - k_y^2), k_z(k_x^2 + k_y^2), k_z^2$
A_2		σ_z		$y(3k_x^2 - k_y^2)$
E		$(k_x, k_y)(\sigma_y, -\sigma_x)$	$(k_x k_y, k_x^2 - k_y^2), (k_z k_x, k_y k_z)$	$\{k_x(k_x^2 + k_y^2), k_y(k_x^2 + k_y^2)\},$ $k_z^2(k_x, k_y),$ $\{k_x k_y k_z, k_z(k_x^2 - k_y^2)\}$

C/NC P/NP	Chiral (C) WPGSs	Non-Chiral (NC) WPGSs
Polar (P) WPGSs	C_1 No constrain	C_s Rashba and Dresselhaus
	C_2 No constrain	C_{2v} Rashba and Dresselhaus
	C_3 Rashba and Weyl	C_{3v} Rashba
	C_4 Rashba and Weyl	C_{4v} Rashba
	C_6 Rashba and Weyl	C_{6v} Rashba
	Non-polar (NP) WPGSs	D_2 Dresselhaus and Weyl
D_3 Weyl		C_{3h} Dresselhaus
D_4 Weyl		D_{2d} Dresselhaus
D_6 Weyl		D_{3h} Dresselhaus
T Weyl		T_d Dresselhaus
O Weyl		

FIG. 3. Classification of the wave vector point group symmetry (WPGS) and the respective linear-in- k Hamiltonian that is symmetrically allowed by the polarity and chirality of the WPGS.

according to the polarity and chirality are classified in four categories, namely, polar chiral (C_1, C_2, C_3, C_4 , and C_6), polar nonchiral ($C_s, C_{2v}, C_{3v}, C_{4v}$, and C_{6v}), nonpolar chiral (D_2, D_3, D_4, D_6, T , and O), and nonpolar nonchiral ($D_{2d}, S_4, C_{3h}, D_{3h}$, and T_d). These four categories are based on the existence of specific proper (rotations) and improper symmetries (reflections and inversion) in the WPGS. Specifically, polar and nonpolar PGs have a single and more than one rotation axis, respectively. On the other hand, chiral PGs have only proper symmetries, while nonchiral have both proper and improper symmetries. Thus, the WPGS classification according to polarity and chirality groups the kind of symmetry operations contained in the WPGS, which has implications in the symmetry-enforced ST shapes. Specifically, we identify two extreme behaviors for the ST, i.e., $\vec{S}_{nk} \perp \vec{k}$ (tangential ST) and $\vec{S}_{nk} \parallel \vec{k}$ (radial ST), resulting from the diagonalization of the Hamiltonians \mathcal{H}_R and \mathcal{H}_W , respectively. The other possible STs are combinations of these two extreme behaviors as in the radial-tangential ST associated to the Hamiltonian \mathcal{H}_D . As summarized in Fig. 3, there is a trend in the symmetrically allowed Hamiltonians for the four WPGS categories: (a) polar chiral WPGS C_3, C_4 , and C_6 symmetrically allow the Hamiltonians \mathcal{H}_R and \mathcal{H}_W , while C_1 and C_2 have no constraints; (b) polar nonchiral WPGS C_{3v}, C_{4v} , and C_{6v} only allow the Rashba Hamiltonian, while polar nonchiral PGs C_s and C_{2v} lead to the SOC terms \mathcal{H}_R and \mathcal{H}_D ; (c) nonpolar chiral WPGS D_3, D_4, D_6, T , and O lead to the SOC term \mathcal{H}_w , but the nonpolar chiral WPGS D_2 leads to both \mathcal{H}_w and \mathcal{H}_D ; and (d) all nonpolar nonchiral WPGS $D_{2d}, S_4, C_{3h}, D_{3h}$, and T_d symmetrically impose the Hamiltonian \mathcal{H}_D . Additional symmetry constraints can be imposed by high-order-in- k SOC terms, which usually result from functions $f_{\gamma m}(k)$ related to d and f functions (e.g., functions in columns with $l > 1$ in Table III).

Since we focus here only on nonmagnetic compounds, i.e., compounds preserving the TR symmetry \mathcal{T} , the ST in anti-ferromagnetic compounds [56] as well as the Zeeman-type effect at k_0 breaking \mathcal{T} [8,9] are not included. Thus, all ST prototypes described above are assumed to intrinsically satisfy the condition $\vec{S}_{n,-k} = \mathcal{T}\vec{S}_{n,k} = -\vec{S}_{n,k}$ (i.e., the pseudovector \vec{S}_{nk} at the inverted k vector is also inverted). In general, the SOC Hamiltonian terms allowed at k_0 [55] intrinsically satisfy the symmetry constraints to the ST, as shown in the next phenomenological discussion.

B. Analysis of how the specific proper and improper symmetry operations determine the direction of the spin-polarization

Using the symmetry constraints imposed by the symmetry operations contained in the WPGS $\mathcal{G}^*(k)$, we identify the allowed spin-polarization patterns in the BZ of NCS compounds. This phenomenological analysis is based on the pseudovector properties of $\langle S_{nk_0}(k) \rangle$.

If a vector property \vec{p} , such as the ferroelectric polarization, is perpendicular to a rotation axis, only R_m with $m = 1$ preserves the crystal unchanged (i.e., rotation of $\theta = 2\pi/m$, which by definition is the identity operation E). Equivalently, if R_m with $m \neq 1$ is a symmetry operation of the crystal, the physical property \vec{p} must be parallel to the rotation axis. The spin-polarization \vec{S}_{nk} is a pseudovector that locally must be parallel to the rotation symmetry operations contained in the WPGS $\mathcal{G}^*(k)$. On the other hand, if a reflection plane M_i is a symmetry operation of $\mathcal{G}^*(k)$, a pseudovector (vector) property \vec{p} must be perpendicular (parallel) to the mirror plane. Thus, \vec{S}_{nk} must be perpendicular to the rotation symmetry operations contained in the WPGS $\mathcal{G}^*(k)$. The SOC Hamiltonian terms symmetrically allowed at k_0 [55] intrinsically satisfy the above-noted constraints imposed by rotations R_m and mirror symmetries M_i in the ST (i.e., $\vec{S}_{nk} \perp M_i$ and $\vec{S}_{nk} \parallel R_i$). Interestingly, the four WPGS categories defined by the polarity and chirality lead to a group of rules (i.e., symmetry constraints) for the spin-polarization vector \vec{S}_{nk_0} , as described in the four respective quadrants (a)–(d) in Fig. 4. To illustrate the relations between categories of little PG symmetry $\mathcal{G}^*(k_0)$ of a wave vector k_0 and the spin-polarization pattern around it, we explain below how simultaneous symmetry restrictions such as $\vec{S}_{nk} \perp M_i$ and $\vec{S}_{nk} \parallel R_i$ can determine the ST described by the specific SOC terms $\mathcal{H}_R, \mathcal{H}_w$, and \mathcal{H}_D :

(a) k -points having polar chiral WPGSs can be characterized by the absence of limiting STs. In the polar chiral WPGS [Fig. 3(a)], there is only one rotation axis R_m (a polar axis). As a result, there are no constraints on the in-plane directions of the polarization \vec{S}_{nk} [Fig. 4(a)]. We refer to this condition as the *absence of pure limiting ST behaviors* [either $\vec{S}_{nk} \perp \vec{k}$ or $\vec{S}_{nk} \parallel \vec{k}$]. Group symmetry analysis indicates that, for C_3, C_4 , and C_6 , the linear-in- k SOC Hamiltonian at k_0 can be written as a superposition of the Rashba \mathcal{H}_R and Weyl \mathcal{H}_w SOC terms [55]. The spin-polarization pattern observed in WPGS $\mathcal{G}^*(k_0) = C_m$ (with $m = 3, 4$, and 6) depends on the strength of Rashba and Weyl SOC terms λ_R and λ_w , respectively (all combinations between λ_R and λ_w are symmetry allowed). Rashba and Weyl SOC intrinsically imposes that, at the rotated momentum vector \vec{k} (i.e., $\hat{R}_m \vec{k}$), the spin-polarization \vec{S}_{nk} near k_0 is also rotated, i.e., $\hat{R}_m \vec{S}_{nk}$ (with \hat{R}_m being the rotation

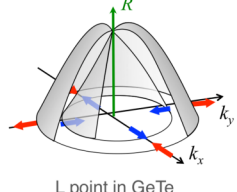
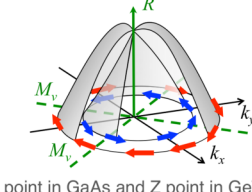
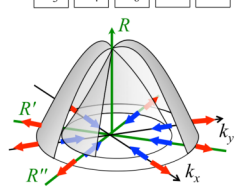
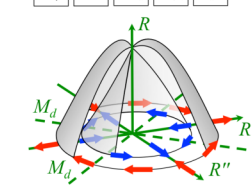
C/NC	Chiral (C)	Non-Chiral (NC)
P/NP	Wavevector point group symmetry	Wavevector point group symmetry
Polar (P)	(a) Undefined ST pattern C_3 C_4 C_6  L point in GeTe	(b) <i>Tangential</i> ST C_{3v} C_{4v} C_{6v}  L point in GaAs and Z point in GeTe
	(c) <i>Radial</i> ST D_3 D_4 D_6 T O  A point in Te and Γ point in OsSi	(d) <i>Tangential-radial</i> ST S_4 C_{3h} D_{2d} D_{3h} T_d  Γ point in GaAs
Non-polar (NP)	Wavevector point group symmetry	Wavevector point group symmetry

FIG. 4. Classification of the wave vector point group symmetry (WPGS) and spin textures (STs) according to the polarity and chirality of the WPGS. Blue and red arrows represent the STs of the inner and outer energy contour of spin split bands. Green solid and green dashed lines stand for the rotation axis and mirror plane projections in a plane perpendicular to the rotation axis, respectively. In each panel, examples of STs at different high-symmetry wave vectors are presented. In the specific case of the WPGSs C_1 and C_2 [polar chiral WPGS—panel (a)], there is no defined ST pattern, as shown in Fig. 3. For C_s (only one mirror plane) and C_{2v} (no mirror planes), which are polar nonchiral WPGSs [panel (b)], a combination of ST prototypes with near zero out-of-plane ST is expected, rather than a perfect tangential ST.

symmetry operator), as required by the existence of the polar axis R_m . In Fig. 4(a), the ST expected in k -points with PGs having rotation symmetry R_4 (i.e., C_4) is illustrated. Due to the absence of limiting behaviors (i.e., pure Rashba or Weyl STs) and possible arbitrary λ_R and λ_w in polar chiral WPGS, there are no defined patterns for the in-plane spin-polarization.

(b) k -points having polar nonchiral WPGS can be characterized by pure Rashba ST. In k_0 with polar nonchiral WPGS [Fig. 3(b)], there is one polar rotation axis R_n and vertical mirror planes (M_v), i.e., planes containing the polar axis. For instance, the $\mathcal{G}^*(k_0) = C_{3v}$ is formed by threefold rotation symmetries R_3 and three vertical mirror planes σ_v (i.e., the planes containing the rotation axis R_3). Thus, \vec{S}_{nk} is required to be perpendicular to the planes M_v [as represented at the green dashed lines in Fig. 4(b)]. Like in polar chiral WPGS, the spin-polarization pattern is also required to satisfy the rotation symmetry at all k -points around the polar axis. Thus, the coexistence of polar rotation symmetries and vertical mirror planes implies that \vec{S}_{nk} is perpendicular to the momentum \vec{k} ($\vec{S}_{nk} \perp \vec{k}$), which is referred to as spin-momentum locking effect. This effect characterizing the Rashba ST is enforced by symmetry rather than a consequence of the magnitude of the SOC or electric dipoles. In summary, non-Sohncke polar PGs are required to have $\vec{S}_{nk} \perp \vec{k}$ —the pure Rashba ST. The

Hamiltonian describing this extreme behavior is then given by the pure Rashba SOC term \mathcal{H}_R .

In actual compounds, high-symmetry k -points having $\mathcal{G}^*(k_0) = C_{3v}, C_{4v}$, and C_{6v} are expected to have this limiting behavior. Examples include $k_0 = L$ in GaAs ($F\bar{4}3m$) and $k_0 = Z$ in GeTe ($R\bar{3}m$), as shown in Figs. 3(c) and 3(e), respectively. Although first predicted for surfaces with perpendicular external field, the Rashba ST has recently been generalized for bulk compounds, which has motivated the search of this compound with large SS [7].

(c) k -points having nonpolar chiral WPGS can be characterized by pure Weyl ST. For $\mathcal{G}^*(k_0) = D_2, D_3, D_4, D_6, T$, or O [Fig. 3(c)], there is a single polar rotation axis R_m and at least one additional rotation axis (R'_m and R''_m) lying in the plane perpendicular to the polar rotation axis R_m . Here, \vec{S}_{nk} is then required to be parallel to the rotation axis R'_m and R''_m [as represented at the green solid lines in Fig. 3(c)]. Additionally, at the rotated momentum \vec{k} (corresponding to $\hat{R}_m \vec{k}$ or $\hat{R}'_m \vec{k}$), the pseudovector \vec{S}_{nk} is also rotated ($\hat{R}_m \vec{S}_{nk}$ or $\hat{R}'_m \vec{S}_{nk}$). The existence of rotation symmetries perpendicular to the polar axis R_m implies that \vec{S}_{nk} is parallel to the momentum \vec{k} (as in $\vec{S}_{nk} \parallel \vec{k}$), as shown in Fig. 3(c). This radial ST [Fig. 1(c)] is locally given by SOC Weyl term \mathcal{H}_w . The Weyl ST is usually associated to topological Weyl semimetal [36,37] and Kramers-Weyl fermions in chiral compounds [10–12].

In actual compounds, high-symmetry k -points having nonpolar chiral WPGS include the Γ and A points in chiral Te bulk [10–12], as well as the Γ point of the insulators OsSi ($P2_13$) and SeF₄ ($P2_12_12_1$). As predicted by our description, these k -points indeed have the Weyl ST [Fig. 2(h)]. In general, all nonpolar chiral compounds can have the Weyl ST prototype around the Γ point (or other k -point whose WPGS = CPGS).

(d) k -points having nonpolar nonchiral WPGS will show a mixture of pure STs. The ST around k -points having WPGS $\mathcal{G}^*(k_0) = D_{2d}, S_4, C_{3h}, D_{3h}$, or T_d can be seen as a combination of the Weyl and Rashba STs, as shown in Fig. 4(d). The reason is that these PGs contain one polar axis (R_m), additional rotation axes (R'_m and R''_m) perpendicular to R_m as required by Weyl ST, and mirror planes as required by Rashba ST. These reflection planes can be perpendicular to the polar rotation axis (horizontal mirror planes M_h) or can bisect the angle between a pair of rotational axes (diagonal mirror planes M_d). Thus, \vec{S}_{nk} is required to be parallel to the in-plane rotation axis R'_m and R''_m and also perpendicular to mirror planes M_d and M_h , leading to a combination of the extreme behaviors $\vec{S}_{nk} \perp \vec{k}$ and $\vec{S}_{nk} \parallel \vec{k}$ (e.g., the Γ point of GaAs, which is described by the SOC term \mathcal{H}_D).

C. Some consequences of the relation between the k -point PG and ST prototypes

The above-noted ST classification and the existence of symmetries of wave vectors k_0 in the BZ lead to the possibility of having more than one spin-polarization prototype pattern in the same compound. Some additional consequences include (i) Compounds without electric dipoles can have the tangential ST (Rashba ST), meaning that contrary to what has been traditionally established, the asymmetry of the electric polarization is not a necessary condition for the Rashba effect

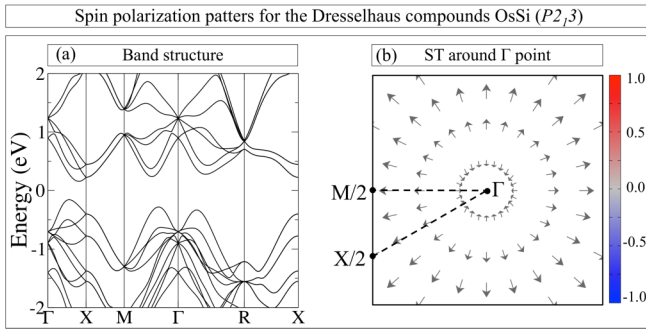


FIG. 5. Relativistic density functional band structure (a) for the “Dresselhaus compound” OsSi ($P2_13$) and (b) spin texture (ST) for the conduction band minimum (CBM) at the Γ point showing typical Weyl-like texture.

[Fig. 2(c)]. (ii) Compounds with electric dipoles can have the Dresselhaus SOC term \mathcal{H}_D at polar chiral WPGS [Fig. 2(f)]. (iii) Spin split bands can have vanishing ST. The tangential-radial ST is not the only way to combine pure Rashba $\vec{s}_{nk} \perp \vec{k}$ and Weyl $\vec{s}_{nk} \parallel \vec{k}$ STs. For instance, when a rotation axis R_m is contained in a diagonal M_d or horizontal M_h mirror plane, the spin-polarization is simultaneously imposed to be parallel and perpendicular to the rotation axis. This contradiction implies that the pseudovector \vec{s}_{nk} must vanish (even in spin split bands), as in 2D SnTe thin film [57]. (iv) Another interesting consequence is the symmetry-enforced radial ST ($\vec{s}_{nk} \parallel \vec{k}$) in bulk compounds. This ST is believed to be a characteristic only linked to symmetry-protected topological phases [36,37]. We find that polar chiral compounds can possess a radial ST $\vec{s}_{nk} \parallel \vec{k}$ at the Γ point, even without a symmetry-protected topological phase. For instance, Fig. 5 shows DFT ST for the valence band maximum at the Γ point of OsSi ($P2_13$). Our finding explains the experimental observation via spin-angle-resolved photoemission spectroscopy of the radial ST in bulk Te [10–12].

Figures 3 and 4 provide a complete classification of the ST in terms of the symmetry conditions intrinsically imposed by WPGSs without symmetry inversion. Although we can directly identify some consequences from the ST classification, the relation between WPGS and ST does not establish all STs that can be found in a single compound with a given CPGS. Indeed, one may erroneously believe that any compound can have any ST shape. In the next section, we thus complete this description by relating the CPGS to a set of symmetrically imposed STs.

V. DESCRIPTION OF THE DPS IMPOSED BY THE WAVE VECTOR PG SYMMETRIES ON THE ST OF A SINGLE COMPOUND

The developed classification for ST shapes for WPGSs without inversion symmetry ratifies that the ST for wave vectors k_0 at which WPGS = CPGS can be predicted by the CPGS. However, this classification does not disclose all ST shapes that can be observed near high-symmetry k -points in the BZ of a given NCS crystalline compound with a specific CPGS \mathcal{G} . This is a fundamental problem for potential spin-

tronic and valleytronic applications. To answer this question, we examine the subgroups for all CPGS \mathcal{G} without inversion symmetry. As very well established, for a given PG \mathcal{G} , there is a limited set of subgroups which are imposed to have lower symmetry than \mathcal{G} , e.g., the subgroups of the PG T_d are C_1 , C_2 , C_s , C_{2v} , C_{3v} , D_2 , T , S_4 , and D_{2d} . Since WPGSs are subgroups of the CPGS (also including the case WPGS = CPGS), the CPGS imposes a limited set of ST shapes in the BZ. The matrix illustrated in Fig. 6 summarizes the symmetrically allowed STs for each CPGS. The columns and lines stand for the CPGS and WPGS classified according to the polarity and chirality, respectively. The matrix component corresponding to the intersection of a CPGS with a WPGS are yellow (gray) when the WPGS is (is not) a subgroup of the CPGS. In other words, the yellow components indicate the WPGS that can exist in the BZ of a compound having any of the considered CPGS. For instance, since the subgroups have lower symmetry than the PG, there is no high-symmetry k -points with WPGS that have larger symmetry than the CPGS, and hence, the lower triangle of the square matrix in Fig. 6 is completely gray. When the WPGS leads to a ST with a defined shape, we include letters indicating the symmetrically allowed linear-in- k SOC Hamiltonians: Rashba (R), Dresselhaus (D), Weyl (W), Rashba and Weyl (RW), Rashba and Dresselhaus (RD), and Weyl and Dresselhaus (WD).

As illustrated in Fig. 6, the DPs for multiple ST shapes in a single compound can be summarized as follows:

(a) Polar chiral CPGS could only have high-symmetry k -points with polar chiral WPGS (first column in Fig. 6). Thus, in compounds with these CPGSs, the ST has no pure limiting ST behaviors [either $\vec{s}_{nk} \perp \vec{k}$ or $\vec{s}_{nk} \parallel \vec{k}$], resulting from the superposition of the SOC terms \mathcal{H}_R and \mathcal{H}_w .

(b) Polar nonchiral CPGS could have high-symmetry k -points with polar WPGS that are chiral and nonchiral (second column in Fig. 6). The tangential ST, imposed by Rashba Hamiltonian \mathcal{H}_R , is thus the only limiting behavior that can be observed in polar nonchiral compounds. In these compounds with CPGSs C_s and C_{2v} , the ST is a combination of the patterns arising from Rashba and Dresselhaus SOC terms ($\mathcal{H}_R + \mathcal{H}_D$). Besides this ST, in polar nonchiral compounds with CPGSs C_{3v} , C_{4v} , and C_{6v} , it is also possible to have a ST arising from the simultaneous presence of Rashba and Weyl SOC terms ($\mathcal{H}_R + \mathcal{H}_w$).

(c) Nonpolar chiral CPGS can have high-symmetry k -points with chiral WPGS that are polar and nonpolar (third column in Fig. 6). The radial ST, imposed by the Weyl Hamiltonian \mathcal{H}_w , is the only limiting behavior in nonpolar chiral compounds. Additionally, compounds with CPGSs D_3 , D_4 , D_6 , T , and O can also have ST arising from the simultaneous presence of Rashba and Weyl SOC terms ($\mathcal{H}_R + \mathcal{H}_w$), as well as Dresselhaus and Weyl SOC terms ($\mathcal{H}_D + \mathcal{H}_w$).

(d) Nonpolar nonchiral CPGS can have WPGS with all possible combinations of polarity and chirality (four column in Fig. 6). The radial-tangential ST can be found in all nonpolar chiral compounds. Additionally, both limiting behaviors for tangential and radial STs could be observed in nonpolar chiral compounds.

According to this description, only polar nonchiral, nonpolar chiral, and nonpolar nonchiral CPGS can have multiple

		Crystal point group symmetry								
		Polar Chiral	Polar Non-Chiral	Non-Polar Chiral	Non-polar Non-Chiral					
		C_1 C_2 C_3 C_4 C_6	C_s C_{2v} C_{3v} C_{4v} C_{6v}	D_2 D_3 D_4 D_6 T O	S_4 C_{3h} D_{2d} D_{3h} T_d					
Wavevector point group symmetry	Polar Chiral	C_1								
		C_2								
		C_3				RW		RW		
		C_4						RW		
		C_6								RW
		C_s								
	Polar Non-Chiral	C_{2v}								
		C_{3v}								
		C_{4v}								
		C_{6v}								
		D_2								
		D_3								
Non-Polar Chiral	D_4									
	D_6									
	T									
	O									
	S_4									
	C_{3h}									
Non-polar Non-Chiral	D_{2d}									
	D_{3h}									
	T_d									
	S_4									
	C_{3h}									
	D_{2d}									

FIG. 6. Classification of crystallographic point group symmetry (CPGS) (columns) and wave vector point group symmetry (WPGS) (lines) according to the polarity and chirality. The intersection between CPGS and WPGS is discriminated by yellow and gray colors. Yellow (gray) means that the specific WPGS is (is not) a subgroup of the CPGS \mathcal{G} , and hence, the WPGS can (cannot) be in the Brillouin zone (BZ) of a compound having crystal point group \mathcal{G} . For each matrix element, we specify the linear-in- k spin-orbit coupling (SOC) Hamiltonian symmetrically allowed by the WPGS: Rashba (R), Dresselhaus (D), Weyl (W), Rashba and Weyl (RW), Rashba and Dresselhaus (RD), and Weyl and Dresselhaus (WD).

STs in the BZ. To illustrate these DPs (a)–(d), we study the DFT-calculated valley-dependent ST in GaAs as represented in Fig. 7. These compounds have T_d CPGS, and hence, the PGs of high-symmetry k -points in the BZ of GaAs correspond to the subgroups of T_d (i.e., C_s , C_2 , C_3 , D_2 , C_{2v} , C_{3v} , D_{2d} , S_4 , and T). However, there is no unequivocal correspondence between the number of high-symmetry k -points and the number of subgroups of the lattice. For instance, high-symmetry k -points Γ , X , L , W , K , and U have PGs T_d , D_{2d} , C_{3v} , S_4 , C_s , and C_s [see Fig. 2(g)], respectively, meaning that there is no k -point in the BZ of GaAs with PG symmetry T , as illustrated by hierarchical decomposition of the subgroups of the PG T_d represented in Fig. 7. The little PGs of k -points impose specific STs, represented only for high-symmetry k -points Γ , X , and L (Fig. 7): the L point is required to have spin-polarization perpendicular to the momentum k ($\vec{S}_{nk} \perp \vec{k}$), and the Γ point can have a mixing of the extreme behaviors $\vec{S}_{nk} \perp \vec{k}$ and $\vec{S}_{nk} \parallel \vec{k}$. In other words, while the Γ point in GaAs has the tangential-radial

ST, as expected, the L point has radiallylike ST [Figs. 2(h) and 2(i)]. Similarly, the high-symmetry points X , W , and K have ST (not shown in Fig. 7) like the one expected at the Γ point.

VI. DFT ILLUSTRATIONS OF THE JOURNEY THROUGH THE BZ AND HIGH-THROUGHPUT CALCULATIONS

The DPs establishing the relationship between each non-magnetic NCS CPGS and the possible ST shapes (Fig. 6) gives the possibility of rationally selecting compounds that have different STs in the BZ. In this section, we apply the previously described theory for the design of compounds that can potentially be used in spintronic devices. Besides the symmetry conditions established in Fig. 6 [i.e., enabling DPs (EDPs)], we also consider DPs for the optimization of the target functionalities, e.g., multiple ST shapes, its position in the BZ, and energy. Optimizing DPs (ODPs) depend on the specific application. Here, we focus on spin-valleytronics, a rapidly growing area based on the use of the spin-polarization

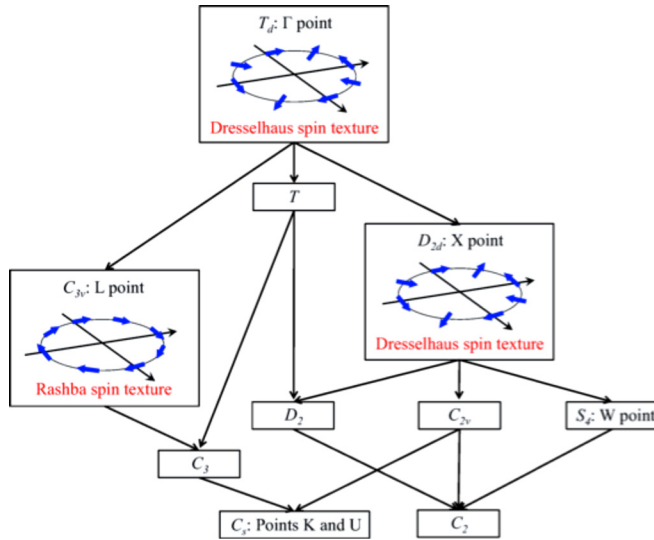


FIG. 7. The Bärnighausen tree provides a hierarchical decomposition of point group (PG) T_d into its subgroups (i.e., C_s , C_2 , C_3 , D_2 , C_{2v} , C_{3v} , D_{2d} , S_4 , and T), e.g., PG T_d can be decomposed in the lower symmetry PGs C_{3v} , D_{2d} , and T . Subgroups T can in turn be decomposed into PGs C_3 and D_2 . For each PG, the high-symmetry k -points are specified, i.e., Γ , X , L , W , K , and U for the PGs T_d , D_{2d} , C_{3v} , S_4 , C_s , and C_3 , respectively. The spin texture expected by the subgroup is represented for Γ , X , and L points.

patterns that are controllable by the degree of freedom of the k valleys in the BZ. Figure 8 summarizes the EDPs for different ST shapes in the same compound as well as ODPs for the control of these STs shapes for spin-valleytronics. Specifically, the starting point is a list of materials that are nonmagnetic and gapped. The EDPs for compounds having multiple ST shapes in the BZ are (i) EDP1: NCS CPGs, and (ii) EDP2: CPGs should also be polar nonchiral, nonpolar chiral, or nonpolar nonchiral. Finally, as we discuss below, the ODP includes ODP1: linear-in- k SSs >1 meV at band edges and k valleys with different WPGs, and ODP2: enough small energy difference between states at different valleys. After selecting compounds using the DPs as filters, we focus on the illustration of some specific prototypes.

A. Inverse design of compounds with multiple ST shapes that can potentially be controlled by the valley degree of freedom

In spin-valleytronics, one wants to have an association between valleys and spin-polarization as established in previous sections based on the WPGs. The basic idea is that, if two high-symmetry k_1 and k_2 points in the BZ have different WPGs, the ST shapes can also be different around these wave vectors. In experiments, k_1 and k_2 can independently be accessed to select different STs. Additionally, since the electronic transport and spin currents are governed by the electronic states near the band edges, the spin currents also depend on the WPGs of the k -point at which the band edges take place. The controllable valley energy requires a sufficiently small energy difference between states at different valleys. The use of this ODP as a filter requires the evaluation of the DFT SOC band structure for a relatively large set of compounds. For this reason, to reduce the computation cost,

before applying the EDPs, we delimit the list of compounds by selecting nonmagnetic gapped materials based on previous DFT calculations without SOC, as described below. Below, we describe the three steps of the materials selection process, namely, materials filtering based on the previous DFT calculations, materials selection based on the symmetry conditions (i.e., enabling DPs), and materials optimization (i.e., optimizing DPs).

1. Find the subset of materials that are nonmagnetic gapped compounds

To reduce the computational cost of high-throughput density functional calculations, we delimit the studied compounds according to their atomic features, i.e., the number of atoms in the unit cell and the orbital type. Our starting point is thus a list from the AFLOW-ICSD database containing 20 831 unique compounds with <20 atoms per unit cell [29] and restricted to atoms having only s , p , and d orbitals. In the AFLOW-ICSD database, there were initially 58 276 entries (32 115 removing duplicated entries). Since we focus on gapped compounds preserving the TR symmetry, we restrict the material selection to nonmagnetic compounds with nonzero bandgap. The screening of nonmagnetic insulators has the bias of the DFT calculations performed in the AFLOW-ICSD database, where the charge density is usually initialized with a ferromagnetic configuration. This could cause antiferromagnetic compounds to be reported as ferromagnetic. In the AFLOW-ICSD database, we use the *spin_cell* feature, which corresponds to the total magnetic moment per unit cell, to filter nonmagnetic compounds. This material screening divides the initial database in two groups: 6993 magnetic materials and 13 838 nonmagnetic compounds. On the other hand, in the AFLOW-ICSD, nonspin-polarized calculations classify compounds as direct gap insulators, indirect gap insulators, metals, and half metals. Based on this classification, the 13 838 nonmagnetic compounds are then divided into 7483 nongapped and 6355 gapped compounds (i.e., band gap >1 meV), as represented in line 1 of Fig. 8. These 6355 nonmagnetic insulator were previously obtained by us [7,20].

2. Find the subset of nonmagnetic gapped compounds that can have different STs in the BZ

We use the crystal PG of the compounds to filter materials satisfying EDP1 and EDP2. Table IV presents the space group index for each CPGs for different polarity, chirality, and Bravais lattices. We notice that there are Bravais lattices with symmetry-forbidden CPGs categories. For instance, in orthorhombic and cubic (triclinic and cubic) lattices, there is no polar chiral (nonchiral) CPGs, and in triclinic and monoclinic (triclinic, monoclinic, orthorhombic, and rhombohedral) lattices, there is no nonpolar chiral (nonchiral) CPGs. All these PGs are necessarily NCS (EDP1 in Fig. 8). We thus filter from the list of nonmagnetic insulators those compounds having NCS CPGs. We find 1709 compounds with NCS CPGs and another list of 4645 compounds with centrosymmetric crystal PGs, as represented in line 2 of Fig. 8. The 1709 compounds with NCS CPGs are divided into 228 polar chiral, 723 polar nonchiral, 253 nonpolar chiral, and 505 nonpolar nonchiral compounds. In previous papers, we studied the SS and fer-

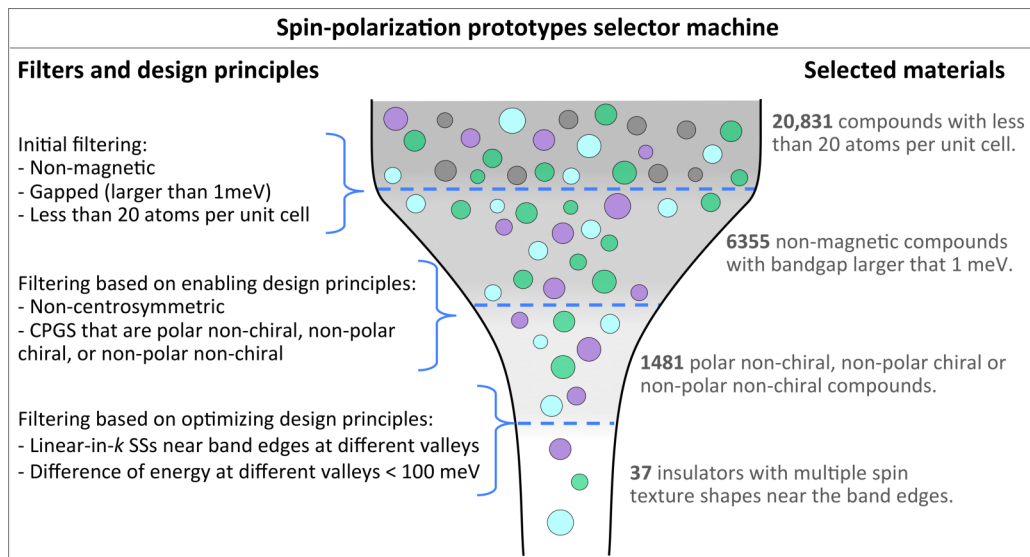


FIG. 8. Data-mining approach to select materials with multiple spin texture shapes near the band edges. The different filters and design principles are indicated in the left, and the number of selected materials for each filter are shown in the right side of the sketch.

roelectric properties of the 951 polar (chiral and nonchiral) compounds [7,8,20]. In Table IV, we specify the abundance of compounds for each NCS CPGS. Curiously, there are no nonmagnetic insulators having the NCS nonpolar chiral CPGS O . Besides the CPGS C_{2v} with 320 compounds, the PGs D_{2d} , T_d , and C_{3v} are the most abundant NCS CPGSs with 194, 183, and 176 compounds, respectively (Table IV). Selecting compounds that can have multiple STs in the BZ (i.e., those with polar nonchiral, nonpolar chiral, or nonpolar nonchiral CPGS), we obtain 1481 compounds (EDP2 in Fig. 8).

Although polar compounds usually have an intrinsic electric polarization, polar CPGS is a necessary but not sufficient condition for electric polarization. The cancelation of dipoles

in polar compounds can be geometrically determined for each atomic site by considering vectors along the atomic bonds. Specifically, the electron transfer given by the atomic bonding of two different elements creates a microscopic dipole whose direction is opposite to the electron transfer direction. For a given atomic site, if all neighbor atoms were locally distributed in such a way that the dipole vectors generated by each bonding cancel each other, then the local atomic site dipole would be zero, e.g., nonpolar atomic sites. Local dipoles can add up to zero for first or second neighbors or be near zero dipole for more distant atomic neighbors (e.g., atomic distances larger than the sum of van der Waals radius for two given elements), which can also be verified

TABLE IV. Space group indexes for 3D Bravais lattices classified according to the inversion symmetry as centrosymmetric, NCS nonpolar, and NCS polar.

Space groups indexes for the 3D Bravais lattices			
		Chiral	Nonchiral
Polar	Triclinic	C_1 : 1 (48)	–
	Monoclinic	C_2 : 3–5 (131)	C_s : 6–9 (112)
	Orthorhombic	–	C_{2v} : 25–46 (320)
	Tetragonal	C_4 : 75–80 (7)	C_{4v} : 99–110 (31)
	Rhombohedral	C_3 : 143–146 (30)	C_{3v} : 156–161 (176)
	Hexagonal	C_6 : 168–173 (12)	C_{6v} : 183–186 (84)
	Cubic	–	–
Nonpolar	Triclinic	–	–
	Monoclinic	–	–
	Orthorhombic	D_2 : 16–24 (88)	–
	Tetragonal	D_4 : 89–98 (22)	S_4 : 81–82 (68)
	Rhombohedral	D_3 : 149–155 (87)	D_{2d} : 111–122 (194)
	Hexagonal	D_6 : 177–182 (18)	–
	Cubic	T : 195–199 (38) O : 207–214 (0)	C_{3h} : 174 (4) D_{3h} : 187–190 (56) T_d : 215–220 (183)

TABLE V. Binary selected compounds with multiple ST shapes in the BZ. The energy difference between states at different valleys is $\Delta_{k_1k_2} = 100$ meV. The space group (SG), SG index, CPGS, and high-symmetry k -points with nonzero SS are given for each compound, as well as the ratio between the SS and momentum offset $\lambda = \Delta_{ss}/k$ (eVÅ). The SOC Hamiltonian predicted by the WPGS (Fig. 3) is given for each high-symmetry k -point.

Material	ICSD	SG index	CPGS	k -point	WPGS	SOC Hamiltonian	SS (meV)	λ (eVÅ)
Bi ₂ O ₃	168 810	$R3m$ (160)	C_{3v}	F	C_{3v}	R	7	0.20
				L	C_s	RD	1	0.06
GeTe	56 040	$R3m$ (160)	C_{3v}	L	C_s	RD	28	3.00
				Z	C_{3v}	R	209	4.25
PbS	183 243	$R3m$ (160)	C_{3v}	L	C_s	RD	20	2.12
				Z	C_{3v}	R	56	1.95
BaTe ₃	36 366	$P\bar{4}2_1m$ (113)	D_{2d}	X	C_{2v}	RD	11	1.09
				G	D_{2d}	D	2	0.26
				Z	D_{2d}	D	23	0.54
Bi ₂ O ₃	41 764	$P\bar{4}2_1c$ (114)	D_{2d}	X	D_2	WD	16	0.40
				G	D_{2d}	D	1	0.09
				R	D_2	WD	13	0.36
Bi ₂ O ₃	168 808	$P\bar{4}m2$ (115)	D_{2d}	X	D_{2d}	D	46	0.37
				R	D_2	WD	36	0.32
B ₂ O ₃	16 021	$P3_121$ (152)	D_3	A	D_3	W	13	0.35
				L	C_2	Undefined	21	0.22
SiO ₂	170 542	$P6_522$ (179)	D_6	M	D_2	WD	3	0.11
				A	D_6	W	26	0.46
				H	D_3	D	6	0.12
BeF ₂	9481	$P6_222$ (180)	D_6	K	D_3	D	1	0.03
				A	D_6	D	6	0.11
				L	D_2	WD	1	0.05
SnI ₄	18 010	$P\bar{4}3m$ (215)	T_d	X	D_{2d}	D	19	0.64
				M	D_{2d}	D	9	0.21
				G	T_d	D	7	0.10
				R	T_d	D	4	0.12
SiO ₂	75 647	$P\bar{4}3m$ (215)	T_d	X	D_{2d}	D	2	0.31
				M	D_{2d}	D	5	0.12
H ₂ O ₂	34 253	$P4_12_12$ (92)	D_4	X	D_2	WD	22	0.32
				Z	D_4	W	4	0.37

geometrically. Thus, polar compounds with nonpolar atomic sites cannot have a total nonzero electric dipole, i.e., nonzero local dipoles can only be found in compounds with polar atomic sites. This gives an intuitive way to verify the local cancelation of dipoles using only the atomic positions and lattice vectors. From the 1481 NCS nonmagnetic insulators, 1018 compounds have at least one polar site. We identify 867 compounds with nonzero dipole and 151 compounds in which local dipoles cancel each other out. The proposed approach based on the geometrical information can result in false positive nonzero dipoles since the electron dipole also depends on the specific chemical species, which requires more exhaustive first-principles calculations. Therefore, we retain this list of 1481 nonmagnetic NCS insulators for our next step.

3. Find the subset of nonmagnetic NCS gapped compounds with ST that can potentially be controlled by the valley

Since controllable valley energy requires a sufficiently small energy difference between states at different valleys $\Delta_{k_1k_2}$, we restrict the material selection based on this ODP (ODP2 in Fig. 8). To evaluate $\Delta_{k_1k_2}$, we perform high-

throughput DFT band structure calculations for the previously selected 1481 nonmagnetic NCS insulators with CPGS allowing multiple ST shapes in the BZ. The DFT calculations with SOC are performed using Perdew-Burke-Ernzenhof generalized gradient approximation [58] as the exchange-correlation functional and the Coulomb self-repulsion onsite term U for transition metals [59] as implemented in the Vienna *Ab initio* Simulation Package (VASP) [60,61]. Based on the high-throughput calculations for the 1481 nonmagnetic NCS insulators that potentially have multiple ST shapes in the BZ, we evaluate the ODPs. We find that there are 64 compounds within ODP1 (i.e., linear-in- k SSs > 1 meV at band edges and k valleys with different CPGS categories). The final number of selected compounds depends on the threshold used for $\Delta_{k_1k_2}$, which in turn depends on the resolution of the measurement and the specific device application. For instance, only 37 compounds have enough small energy difference between states at different valleys (ODP2), when we use $\Delta_{k_1k_2} = 100$ meV. Tables V and VI show the experimentally synthesized compounds at the convex hull (i.e., energy above the convex hull equal to zero $E_{ch} = 0$ meV) obtained in the inverse design process. For each compound, we present the ICSD code,

TABLE VI. Ternary selected compounds with multiple ST shapes in the BZ. The energy difference between states at different valleys is $\Delta_{k_1 k_2} = 100$ meV. The space group (SG), SG index, CPGS, and high-symmetry k -points with nonzero SS are given for each compound, as well as the ratio between the SS and momentum offset $\lambda = \Delta_{ss}/k$ (eVÅ). The SOC Hamiltonian predicted by the WPGS (Fig. 3) is given for each high-symmetry k -point.

Material	ICSD	SG index	CPGS	k -point	WPGS	SOC Hamiltonian	SS (meV)	α_R (eVÅ)
Nb ₃ Sb ₂ Te ₅	417 101	$I\bar{4}3m$ (217)	T_d	H	T_d	D	6	0.23
				N	C_{2v}	RD	24	0.86
AsSe ₃ Tl ₃	15 148	$R3m$ (160)	C_{3v}	L	C_s	RD	77	1.22
				Z	C_{3v}	R	12	0.53
LaTiO ₃	200 088	$P6_3mc$ (186)	C_{6v}	M	C_{2v}	RD	8	1.06
				G	C_{6v}	R	8	0.56
Ag ₅ SbS ₄	16 987	$Cmc2_1$ (36)	C_{2v}	S	C_2	Undefined	5	0.67
				G	C_{2v}	RD	3	0.41
				Y	C_{2v}	RD	10	0.39
BaZnF ₄	182 605	$Cmc2_1$ (36)	C_{2v}	R	C_2	Undefined	2	0.24
				Y	C_{2v}	RD	9	0.11
BaF ₄ Zn	402 926	$Cmc2_1$ (36)	C_{2v}	R	C_2	Undefined	2	0.23
				Y	C_{2v}	RD	10	0.13
ClMnO ₃	416 749	$Cmc2_1$ (36)	C_{2v}	G	C_{2v}	RD	2	0.06
				$A1$	C_2	Undefined	2	0.06
LaTaO ₄	97 688	$Cmc2_1$ (36)	C_{2v}	R	C_2	Undefined	40	0.48
				G	C_{2v}	RD	1	0.03
				$A1$	C_2	Undefined	31	0.37
Na ₂ PtS ₂	87 219	$Cmc2_1$ (36)	C_{2v}	S	C_2	Undefined	1	0.11
				R	C_2	Undefined	10	0.70
				G	C_{2v}	RD	7	0.14
Na ₂ PtSe ₂	40 429	$Cmc2_1$ (36)	C_{2v}	Y	C_{2v}	RD	1	0.07
				S	C_2	Undefined	1	0.09
				R	C_2	Undefined	9	0.85
AgC ₂ N ₃	843	$P3_121$ (152)	D_3	Y	C_{2v}	RD	1	0.09
				L	C_2	Undefined	1	0.09
				M	C_2	Undefined	1	0.09
AlAsO ₄	33 834	$P3_121$ (152)	D_3	G	D_3	W	2	0.56
				A	D_3	W	2	0.61
				L	C_2	Undefined	22	0.15
BF ₄ Li	171 375	$P3_121$ (152)	D_3	A	D_3	W	5	0.10
				L	C_2	Undefined	6	0.06
				G	D_3	W	8	0.17
BaZnO ₂	25 812	$P3_121$ (152)	D_3	M	C_2	Undefined	1	0.05
				A	D_3	W	4	0.34
				G	D_3	W	9	0.19
CsNO ₂	50 327	$P3_121$ (152)	D_3	L	C_2	Undefined	13	0.79
				L	C_2	Undefined	1	0.10
				G	D_3	W	5	1.02
NTiO ₂	50 325	$P3_121$ (152)	D_3	L	C_2	Undefined	1	0.13
				H	D_3	W	6	1.10
				G	D_3	W	10	1.94
CaIr ₂ P ₂	95 756	$P3_221$ (154)	D_3	A	D_3	W	80	0.83
				G	D_3	W	40	0.96
				M	C_2	Undefined	77	0.85
SrIr ₂ P ₂	73 531	$P3_221$ (154)	D_3	G	D_3	W	53	0.96
				M	C_2	Undefined	87	0.84
				M	C_2	Undefined	87	0.84
LaPO ₄	31 564	$P6_222$ (180)	D_6	M	D_2	WD	3	0.49
				A	D_6	W	4	0.14
				A	D_6	W	4	0.14
Hg ₃ Te ₂ Br ₂	27 402	$I2_13$ (199)	T	N	C_2	Undefined	6	0.56
				G	T	W	10	0.27
Cl ₂ Hg ₃ S ₂	28 159	$I2_13$ (199)	T	G	T	W	3	0.14
				N	C_2	Undefined	4	0.17
Cl ₂ Hg ₃ Te ₂	27 401	$I2_13$ (199)	T	G	T	W	9	0.31
				N	C_2	Undefined	32	0.68
PtSnTh	108 712	$F\bar{4}3m$ (216)	T_d	G	T_d	D	4	0.33
				X	D_{2d}	D	6	0.76
GaPO ₄	30 881	$P3_121$ (152)	D_3	G	D_3	W	2	0.54
				L	C_2	Undefined	3	0.17
GaPO ₄	33 253	$P3_121$ (152)	D_3	G	D_3	W	2	0.50
				L	C_2	Undefined	3	0.17

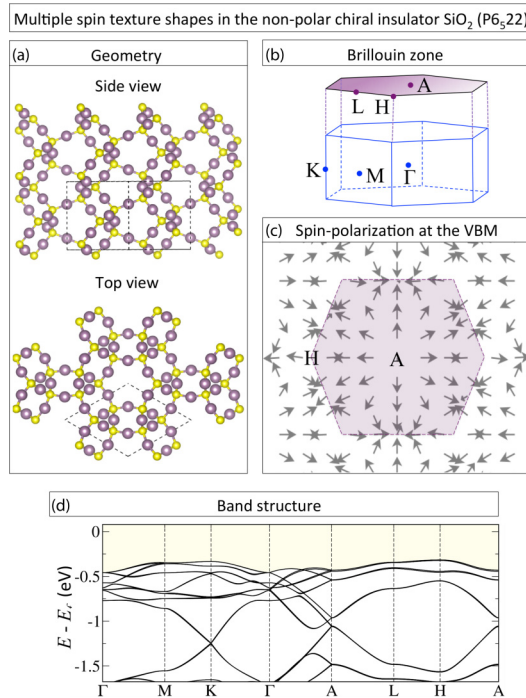


FIG. 9. Multiple spin texture shapes in the non-polar chiral insulator SiO_2 ($P6_522$). (a) Top and side view of SiO_2 . Silicon and Oxygen atoms are represented in yellow and purple, respectively. (b) Brillouin zone for the chiral SiO_2 . The two-dimensional hexagonal projection of the plane containing the high symmetry k -points A and H is shown in purple. (c) Spin-polarization at the valence band maximum (VBM) at the two-dimensional projection in (b). Around A, the radial ST is observed, while the tangential-radial ST is found around H. The hexagonal BZ is delimited by the purple region. The arrows stand for the in-plane spin-polarization components and the out-plane spin-component S_z is always zero. (d) DFT calculated valence bands for SiO_2 ($P6_522$).

energy above the convex hull (E_{ch}) given by the materials project (meV/fu), SS in meV, and R-factor for refinement of the experimental structure. The double entries stand for compounds with the same atomic composition but different ICSD number and different SS.

B. Discussion of the predicted compounds for potential spin-valleytronics applications

The list of compounds identified to have multiple ST shapes in the BZ includes known ferroelectrics as GeTe and 36 previously synthesized compounds potentially allowing the spin-polarization control based on the k -valley energy. Tables V and VI show the 12 binary and 25 ternary rationally selected compounds. Here, we explore in detail some of these compounds.

Our inverse design approach confirms the multiple STs in GeTe (Rashba Hamiltonian at the Z and Rashba-Dresselhaus Hamiltonian at the A point), which is very well known be-

cause of its ferroelectric properties [13,19,25] (Table V). We find other fabricated compounds with giant SS near band edges. For example, AsSe_3Te_3 and SrIr_2P_2 have SS > 70 and 80 meV, respectively. While AsSe_3Te_3 has Rashba and Rashba-Dresselhaus STs at the Z and L high-symmetry k -points, respectively, in SrIr_2P_2 , the Weyl ST is found at the Γ point and an undefined ST at the M point (Table VI). On the other hand, the DFT-calculated Weyl, Rashba, and Dresselhaus coefficients (λ_W , λ_R , and λ_D) are usually small (< 1 eV/Å). Indeed, only a few compounds have large λ coefficients, e.g., NTiO_2 with Weyl coefficient λ_W of 1.94 eV/Å at the Γ point and 1.10 eV/Å at the high-symmetry point H. A remarkable example of a very well-known compound with relatively weak SOC is the nonpolar chiral SiO_2 ($P6_522$), CPGS = D_6 , that has radial ST at the high-symmetry point A (WPGS = CPGS) and tangential-radial ST at the high-symmetry point H (WPGS = D_3), as shown in Fig. 9. The SSs at these k -points are 26 and 6 meV, respectively.

VII. CONCLUSIONS

Despite the fact that the CPGS (e.g., absence or presence of electric dipoles) does not unequivocally determine the ST, we find that the WPGS $\mathcal{G}^*(k_0)$ can be a descriptor for this functionality. The important consequence of this discovery is that the selectivity in types of STs can be rationalized based on symmetry (neither spin-orbit physics nor the mere existence of electric fields/dipoles), and therefore, the ST can be designed. These consequences are extended to other spin-related phenomena. For instance, the spin-momentum locking effect is enforced by symmetry, rather than a consequence of strong SOC or topological effects. Additionally, our findings suggest the possibility of accessing different STs in the same compound by controlling the relative energy position of states in different valleys of the BZ, which has potential application for spin-valleytronics. We use the symmetry conditions defining the ST to establish all possible ST prototypes in the 21 NCS CPGSs for 3D crystals. Using these symmetry relations as DPs, we select 1481 compounds from the AFLOW-ICSD database [29]. Performing DFT band structure calculations for the selected compounds, we predict 37 materials unnoticed to have multiple ST shapes at different k valleys. The ST symmetry classification as well as the predicted compounds with multiple ST can be a platform for potential application for the control of the ST by accessing different valleys.

ACKNOWLEDGMENTS

The work at the University of Colorado at Boulder was supported by the National Science Foundation (NSF) Grant No. NSF-DMR-CMMT and No. DMR-1724791. CMA and GMD are supported by the São Paulo Research Foundation (FAPESP) Grant No. 18/11856-7, No. 19/03663-7, and No. 17/02317-2. High-throughput calculations were performed at the Santos Dumont supercomputer (LNCC/Brazil).

[1] D. B. Litvin, Ferroelectric space groups, *Acta Crystallogr. A* **42**, 44 (1986).

[2] N. A. Spaldin, *Magnetic Materials: Fundamentals and Applications*, 2nd ed. (Cambridge University Press, Cambridge, 2010).

- [3] W. C. Johnson, Protein secondary structure and circular dichroism: a practical guide, *Proteins* **7**, 205 (1990).
- [4] M. Nespolo, M. I. Aroyo, and B. Souvignier, Crystallographic shelves: space-group hierarchy explained, *J. Appl. Crystallogr.* **51**, 1481 (2018).
- [5] B. Bradlyn, J. Cano, Z. Wang, M. G. Vergniory, C. Felser, R. J. Cava, and B. A. Bernevig, Beyond Dirac and Weyl fermions: unconventional quasiparticles in conventional crystals, *Science* **353**, aaf5037 (2016).
- [6] A. A. Soluyanov, D. Gresch, Z. Wang, Q. Wu, M. Troyer, X. Dai, and B. A. Bernevig, Type-II Weyl semimetals, *Nature* **527**, 495 (2015).
- [7] C. M. Acosta, E. Ogoshi, A. Fazzio, G. Dalpian, and A. Zunger, The Rashba scale: Emergence of band anti-crossing as a design principle for materials with large Rashba coefficient, *Matter* **3**, 145 (2020).
- [8] C. Mera Acosta, A. Fazzio, and G. M. Dalpian, Zeeman-type spin splitting in nonmagnetic three-dimensional compounds, *Npj Quantum Mater.* **4**, 41 (2019).
- [9] H. Yuan, M. S. Bahramy, K. Morimoto, S. Wu, K. Nomura, B.-J. Yang, H. Shimotani, R. Suzuki, M. Toh, C. Kloc, X. Xu, R. Arita, N. Nagaosa, and Y. Iwasa, Zeeman-type spin splitting controlled by an electric field, *Nat. Phys.* **9**, 563 (2013).
- [10] M. Sakano *et al.*, Radial Spin Texture in Elemental Tellurium with Chiral Crystal Structure, *Phys. Rev. Lett.* **124**, 136404 (2020).
- [11] G. Gatti *et al.*, Radial Spin Texture of the Weyl Fermions in Chiral Tellurium, *Phys. Rev. Lett.* **125**, 216402 (2020).
- [12] T. Yoda, T. Yokoyama, and S. Murakami, Current-Induced orbital and spin magnetizations in crystals with helical structure, *Sci. Rep.* **5**, 12024 (2015).
- [13] D. Di Sante, P. Barone, R. Bertacco, and S. Picozzi, Electric control of the giant Rashba effect in bulk GeTe, *Adv. Mater.* **25**, 509 (2013).
- [14] J. Krempaský, S. Muff, J. Minár, N. Pilet, M. Fanciulli, A. P. Weber, E. B. Guedes, M. Caputo, E. Müller, V. V. Volobuev, M. Gmitra, C. A. F. Vaz, V. Scagnoli, G. Springholz, and J. H. Dil, *Operando* Imaging of All-Electric Spin Texture Manipulation in Ferroelectric and Multiferroic Rashba Semiconductors, *Phys. Rev. X* **8**, 021067 (2018).
- [15] K. Ishizaka *et al.*, Giant Rashba-type spin splitting in bulk BiTeI, *Nat. Mater.* **10**, 521 (2011).
- [16] M. Kobayashi, I. Muneta, T. Schmitt, L. Patthey, S. Ohya, M. Tanaka, M. Oshima, and V. N. Strocov, Digging up bulk band dispersion buried under a passivation layer, *Appl. Phys. Lett.* **101**, 242103 (2012).
- [17] Z. Liu, S. Thirupathiah, A. N. Yaresko, S. Kushwaha, Q. Gibson, W. Xia, Y. Guo, D. Shen, R. J. Cava, and S. V. Borisenko, A giant bulk-type Dresselhaus splitting with 3D chiral spin texture in IrBiSe, *Phys. Status Solidi RRL* **14**, 1900684 (2020).
- [18] I.-H. Park, Q. Zhang, K. C. Kwon, Z. Zhu, W. Yu, K. Leng, D. Giovanni, H. S. Choi, I. Abdelwahab, Q.-H. Xu, T. C. Sum, and K. P. Loh, Ferroelectricity and Rashba effect in a two-dimensional Dion-Jacobson hybrid organic-inorganic perovskite, *J. Am. Chem. Soc.* **141**, 15972 (2019).
- [19] M. Liebmann *et al.*, Giant Rashba-type spin splitting in ferroelectric GeTe(111), *Adv. Mater.* **28**, 560 (2016).
- [20] C. M. Acosta, A. Fazzio, G. M. Dalpian, and A. Zunger, Inverse design of compounds that have simultaneously ferroelectric and Rashba cofunctionality, *Phys. Rev. B* **102**, 144106 (2020).
- [21] L. Seixas, D. West, A. Fazzio, and S. B. Zhang, Vertical twinning of the Dirac cone at the interface between topological insulators and semiconductors, *Nat. Commun.* **6**, 7630 (2015).
- [22] L. C. Lew Yan Voon and M. Willatzen, *The $k \cdot p$ Method: Electronic Properties of Semiconductors* (Springer, Dordrecht, New York, 2009).
- [23] M. S. Dresselhaus, A. Jorio, and G. Dresselhaus, *Group Theory: Application to the Physics of Condensed Matter* (Springer-Verlag, Berlin, Heidelberg, 2008).
- [24] A. Manchon, H. C. Koo, J. Nitta, S. M. Frolov, and R. A. Duine, New perspectives for Rashba spin-orbit coupling, *Nat. Mater.* **14**, 871 (2015).
- [25] L. Ponet and S. Artyukhin, First-principles theory of giant Rashba-like spin splitting in bulk GeTe, *Phys. Rev. B* **98**, 174102 (2018).
- [26] K. V. Shanavas, Overview of theoretical studies of Rashba effect in polar perovskite surfaces, *J. Electron Spectrosc. Relat. Phenom.* **201**, 121 (2015).
- [27] W. Lin, L. Li, F. Doğan, C. Li, H. Rotella, X. Yu, B. Zhang, Y. Li, W. S. Lew, S. Wang, W. Prellier, S. J. Pennycook, J. Chen, Z. Zhong, A. Manchon, and T. Wu, Interface-based tuning of Rashba spin-orbit interaction in asymmetric oxide heterostructures with 3d Electrons, *Nat. Commun.* **10**, 3052 (2019).
- [28] A. Zunger, Inverse design in search of materials with target functionalities, *Nat Rev Chem* **2**, 0121 (2018).
- [29] S. Curtarolo, W. Setyawan, G. L. W. Hart, M. Jainatek, R. V. Chepulskii, R. H. Taylor, S. Wang, J. Xue, K. Yang, O. Levy, M. J. Mehl, H. T. Stokes, D. O. Demchenko, and D. Morgan, AFLOW: An automatic framework for high-throughput materials discovery, *Comput. Mater. Sci.* **58**, 218 (2012).
- [30] E. I. Rashba, Properties of semiconductors with an extremum loop. I. Cyclotron and combinational resonance in a magnetic field perpendicular to the plane of the loop, *Soviet Physics, Solid State* **2**, 1109 (1960).
- [31] E. I. Rashba and V. I. Sheka, Simmetriya Energeticheskikh Zon v Kristallakh Tipa Vyurtsita. II. Simmetriya Zon s Uchytotom Spinovykh Vzaimodeistvii, *Fizika Tverd. Tela*, Collected Papers (Leningrad) **1**, 162 (1959).
- [32] Yu. A. Bychkov and E. I. Rashba, Properties of a 2D electron gas with lifted spectral degeneracy, *JETP Lett.* **39**, 78 (1984).
- [33] M. S. Bahramy, R. Arita, and N. Nagaosa, Origin of giant bulk Rashba splitting: Application to BiTeI, *Phys. Rev. B* **84**, 041202(R) (2011).
- [34] M. Z. Hasan and C. L. Kane, Colloquium: Topological insulators, *Rev. Mod. Phys.* **82**, 3045 (2010).
- [35] H. Weyl, Elektron und Gravitation. I, *Z. Physik* **56**, 330 (1929).
- [36] B. Yan and C. Felser, Topological materials: Weyl semimetals, *Annu. Rev. Condens. Matter Phys.* **8**, 337 (2017).
- [37] N. P. Armitage, E. J. Mele, and A. Vishwanath, Weyl and Dirac semimetals in three-dimensional solids, *Rev. Mod. Phys.* **90**, 015001 (2018).
- [38] G. Dresselhaus, Spin-orbit coupling effects in zinc blende structures, *Phys. Rev.* **100**, 580 (1955).
- [39] L. P. Bouckaert, R. Smoluchowski, and E. Wigner, Theory of Brillouin zones and symmetry properties of wave functions in crystals, *Phys. Rev.* **50**, 58 (1936).
- [40] R. J. Elliott, Spin-orbit coupling in band theory—character tables for some “double” space groups, *Phys. Rev.* **96**, 280 (1954).

- [41] J. C. Slater, Space groups and wave-function symmetry in crystals, *Rev. Mod. Phys.* **37**, 68 (1965).
- [42] S.-H. Wei and A. Zunger, Electronic and structural anomalies in lead chalcogenides, *Phys. Rev. B* **55**, 13605 (1997).
- [43] B. Bradlyn, L. Elcoro, J. Cano, M. G. Vergniory, Z. Wang, C. Felser, M. I. Aroyo, and B. A. Bernevig, Topological quantum chemistry, *Nature* **547**, 298 (2017).
- [44] M. G. Vergniory, L. Elcoro, C. Felser, N. Regnault, B. A. Bernevig, and Z. Wang, A complete catalogue of high-quality topological materials, *Nature* **566**, 480 (2019).
- [45] J. Kruthoff, J. de Boer, J. van Wezel, C. L. Kane, and R.-J. Slager, Topological Classification of Crystalline Insulators through Band Structure Combinatorics, *Phys. Rev. X* **7**, 041069 (2017).
- [46] C. M. Acosta and A. Fazzio, Spin-Polarization Control Driven by a Rashba-Type Effect Breaking the Mirror Symmetry in Two-Dimensional Dual Topological Insulators, *Phys. Rev. Lett.* **122**, 036401 (2019).
- [47] S. Picozzi, Ferroelectric Rashba semiconductors as a novel class of multifunctional materials, *Front. Physics* **2**, 10 (2014).
- [48] D. Khokhriakov, A. W. Cummings, K. Song, M. Vila, B. Karpiak, A. Dankert, S. Roche, and S. P. Dash, Tailoring emergent spin phenomena in Dirac material heterostructures, *Sci. Adv.* **4**, eaat9349 (2018).
- [49] X. Zhang, Q. Liu, J.-W. Luo, A. J. Freeman, and A. Zunger, Hidden spin polarization in inversion-symmetric bulk crystals, *Nat. Phys.* **10**, 387 (2014).
- [50] J. Zak, Symmetry Specification of Bands in Solids, *Phys. Rev. Lett.* **45**, 1025 (1980).
- [51] J. Zak, Band representations and symmetry types of bands in solids, *Phys. Rev. B* **23**, 2824 (1981).
- [52] J. Zak, Selection rules for localized states in solids: application to band calculations, *Phys. Rev. B* **26**, 1959 (1982).
- [53] S. L. Altmann and P. Herzig, *Point-Group Theory Tables* (Clarendon Press, Oxford University Press, Oxford, New York, 1994).
- [54] C. R. Ast and I. Gierz, *sp*-band tight-binding model for the Bychkov-Rashba effect in a two-dimensional electron system including nearest-neighbor contributions from an electric field, *Phys. Rev. B* **86**, 085105 (2012).
- [55] Sz. Vajna, E. Simon, A. Szilva, K. Palotas, B. Ujfalussy, and L. Szunyogh, Higher-order contributions to the Rashba-Bychkov effect with application to the Bi/Ag(111) surface alloy, *Phys. Rev. B* **85**, 075404 (2012).
- [56] L.-D. Yuan, Z. Wang, J.-W. Luo, E. I. Rashba, and A. Zunger, Giant momentum-dependent spin splitting in centrosymmetric low-*z* antiferromagnets, *Phys. Rev. B* **102**, 014422 (2020).
- [57] K. Liu, W. Luo, J. Ji, P. Barone, S. Picozzi, and H. Xiang, Band splitting with vanishing spin polarizations in noncentrosymmetric crystals, *Nat. Commun.* **10**, 5144 (2019).
- [58] J. P. Perdew, K. Burke, and M. Ernzerhof, Generalized Gradient Approximation Made Simple, *Phys. Rev. Lett.* **77**, 3865 (1996).
- [59] A. I. Liechtenstein, V. I. Anisimov, and J. Zaanen, Density-functional theory and strong interactions: orbital ordering in Mott-Hubbard insulators, *Phys. Rev. B* **52**, R5467 (1995).
- [60] G. Kresse and J. Furthmüller, Efficient iterative schemes for *ab initio* total-energy calculations using a plane-wave basis set, *Phys. Rev. B* **54**, 11169 (1996).
- [61] G. Kresse and D. Joubert, From ultrasoft pseudopotentials to the projector augmented-wave method, *Phys. Rev. B* **59**, 1758 (1999).